

---

# A fully-differentiable compressible high-order computational fluid dynamics solver

---

**Deniz A. Bezgin\***

Chair of Aerodynamics and Fluid Mechanics  
Technical University of Munich  
D-85748 Garching bei Muenchen  
deniz.bezgin@tum.de

**Aaron B. Buhendwa\***

Chair of Aerodynamics and Fluid Mechanics  
Technical University of Munich  
Garching bei Muenchen  
aaron.buhendwa@tum.de

**Nikolaus A. Adams**

Chair of Aerodynamics and Fluid Mechanics  
Technical University of Munich  
Garching bei Muenchen  
nikolaus.adams@tum.de

## Abstract

Fluid flows are omnipresent in nature and engineering disciplines. The reliable computation of fluids has been a long-lasting challenge due to nonlinear interactions over multiple spatio-temporal scales. The compressible Navier-Stokes equations govern compressible flows and allow for complex phenomena like turbulence and shocks. Despite tremendous progress in hardware and software, capturing the smallest length-scales in fluid flows still introduces prohibitive computational cost for real-life applications. We are currently witnessing a paradigm shift towards machine learning supported design of numerical schemes as a means to tackle aforementioned problem. While prior work has explored differentiable algorithms for one- or two-dimensional incompressible fluid flows, we present a fully-differentiable three-dimensional framework for the computation of compressible fluid flows using high-order state-of-the-art numerical methods. Firstly, we demonstrate the efficiency of our solver by computing classical two- and three-dimensional test cases, including strong shocks and transition to turbulence. Secondly, and more importantly, our framework allows for end-to-end optimization to improve existing numerical schemes inside computational fluid dynamics algorithms. In particular, we are using neural networks to substitute a conventional numerical flux function.

## 1 Intro

Fluid flows are omnipresent in nature and engineering disciplines with applications reaching from the design of combustion-engines and windturbines, the simulation of climate and weather forecasts, to magnetohydrodynamics in plasma physics. The accurate simulation and the development of high-fidelity models for such flows has been a long-standing challenge in computational fluid mechanics.

In the past few years machine learning has been extensively used in engineering disciplines and physical sciences alike. ML methods have the capabilities to learn complex relations from data and enable novel modeling strategies as well as new avenues of postprocessing. Amongst others, the intersection of machine learning and fluid mechanics has experienced renewed interest [1]. A

---

\*D.A.B. and A.B.B. contributed equally to this work.

multitude of research has put forward different ways of using ML in scientific applications. These methods can be categorized according to different criteria. One important distinction is the ratio of physical prior-knowledge to "pure ML" that is included in model and training. While pure ML schemes have the advantage of being efficient and quickly implemented, they do not offer guarantees on performance (e.g. convergence or stability). Since they do not include the underlying physics, it is often difficult to enforce constraints such as symmetry or conservation of energy. In contrast, established numerical methods often come with guarantees on convergence and error bounds, and a plethora of research has investigated the hybridization of ML and classical numerics.

A second major distinction of ML models can be made according to on- and offline training. Up until now, ML models have been typically optimized offline, i.e. outside of a simulator. Upon proper training, they are then plugged in the solver for evaluation of down-stream tasks. Examples include training of explicit subgrid scale models in large eddy simulations [2], interface reconstruction in multiphase flows [3, 4], and cell-face reconstruction in shock-capturing schemes [5, 6]. However, the successful development of powerful general-purpose automatic-differentiation frameworks, such as Tensorflow [7], Pytorch [8], and JAX [9] has enabled online training of ML models. Models are optimized end-to-end within a differentiable simulator or program. This has two significant advantages: the ML model observes the dynamics of the underlying physics and sees its own outputs as inputs. In this fashion, Bar-Sinai et al. [10] have proposed data-driven discretizations for one- and two-dimensional PDEs while Bezzin et al. [11] have trained a subgrid-scale closure for nonclassical shocks. More recently, Schoenholz and Cubuk have put forward JAX-MD [12], a differentiable software package for molecular dynamics. An exciting work in the direction of fluid mechanics is JAX-CFD [13] which is an ML-accelerated fluid dynamics simulator for incompressible two-dimensional flows. JAX-CFD has been successfully used to learn data-driven turbulence models for two-dimensional turbulent flows.

Inspired by these previous works, we introduce a fully differentiable high-order computational fluid dynamics solver for the compressible Navier-Stokes equations. As previous works have focused on one- or two-dimensional systems, our framework allows for the simulation of the three-dimensional compressible Navier-Stokes equations. Compressible flows are challenging as they feature not only chaotic turbulent behavior but may also be shock-dominated. Suitable numerical methods, therefore, have to be capable of resolving small-scale flow features and of shock capturing. These at times contradictory requirements have been a long-lasting challenge and require novel solution which we want to explore with differentiable simulators. Therefore, our numerical solver is completely written in JAX - a language that supports reverse-mode automatic differentiation. This allows us end-to-end training of ML models like neural-networks within the solver.

In the following we detail physical and numerical aspects of the fluid solver alongside important design and programming aspects. We demonstrate the efficiency of the forward-pass through our solver. Finally, we illustrate how our framework can be used for exploration of data-driven numerical schemes.

## 2 CFD: Physical and numerical models

### 2.1 Governing equation

A general differential conservation law for the state vector  $\mathbf{U}$  can be written in symbolic notation as

$$\frac{\partial \mathbf{U}}{\partial t} = -\nabla \mathbf{F}(\mathbf{U}) + S(\mathbf{U}), \quad (1)$$

where  $\mathbf{F}(\mathbf{U})$  and  $S(\mathbf{U})$  are the flux vector and the source term vector [14]. For the compressible Navier-Stokes equations, the state vector of conservative variables  $\mathbf{U} = (\rho, \rho u, \rho v, \rho w, E)^T$ . Here,  $\rho$  is the density,  $u, v, w$  are the velocity components in the spatial directions  $x, y, z$ , respectively, and  $E$  is the total energy. A different representation of the state is given by the vector of primitive variables  $\mathbf{W} = (\rho, u, v, w, p)^T$ , with the pressure  $p$ . The total energy is given by  $E = \rho e + \frac{1}{2}\rho(u^2 + v^2 + w^2)$ , with the internal energy per unit mass  $e$ . An equation of state is needed to close the system of equations. In this work, we choose the equation of state for an ideal gas,  $e = p / ((\gamma - 1)\rho)$  with the ratio of specific heats  $\gamma$ . We set  $\gamma = 1.4$  if not stated otherwise.

---

**Algorithm 1** Simplified compute loop for Euler method.

---

**Require:**  $U^n, t_{end}$   
**while**  $t < t_{end}$  **do**  
     $\Delta t \leftarrow \text{compute\_time\_step}(U^n)$   
     $U_{rhs}^n \leftarrow \text{compute\_right\_hand\_side}(U^n)$   
     $U^n \leftarrow \text{integrate}(U^n, U_{rhs}^n, \Delta t)$   
     $U^n \leftarrow \text{fill\_boundaries}(U^n)$   
     $t \leftarrow t + \Delta t$   
**end while**

---



---

**Algorithm 2** Simplified algorithm to compute the right hand side.

---

**Require:**  $U^n$   
     $U_L^n, U_R^n \leftarrow \text{reconstruct\_cell\_face\_values}(U^n)$   
     $W_L^n, W_R^n \leftarrow \text{compute\_primitives\_from\_conservatives}(U^n)$   
     $F^n \leftarrow \text{solve\_riemann\_problem}(U_L^n, U_R^n, W_L^n, W_R^n)$   
     $U_{rhs}^n \leftarrow F^n$

---

For the Navier-Stokes equations, the source term vector includes viscous forces, heat conduction, and gravitational forces, amongst others. For  $S(U) = 0$ , we recover the Euler equations which are a set of hyperbolic differential equations [14].

## 2.2 Architecture

We solve the compressible Navier-Stokes equations using finite volumes on a Cartesian mesh with cubic cells in 3D. The simplified compute loop of our code is depicted in algorithm 1. Starting from the initial vector of conservatives  $U_0 = U(t_0)$  at time  $t_0$ , integration steps are performed until the final time  $t_{end}$  is reached. A single integration step consists mainly of the right hand side evaluation of Eq. (1) and subsequent integration of the vector of conservatives. The majority of compute time is spent in `compute_right_hand_side( $U^n$ )`. Here, the general procedure consists of the left and right sided cell-face reconstruction  $U_L, U_R$  and subsequent evaluation of the cell-face Riemann problem, yielding the cell-face flux  $F^n$  (compare algorithm 2).

In literature, there exists a wide variety of different time integrators, cell-face reconstruction schemes, and approximate Riemann solvers [14]. We use a modular, object-oriented programming framework which allows for convenient exchange of submodules, i.e. time integration schemes, cell-face reconstruction schemes, and Riemann solvers. Before running the simulator, the user specifies the numerical setup. We focus on state-of-the-art high-order shock-capturing methods. Explicit total-variation-diminishing (TVD) Runge-Kutta integrators up to order 3 and the classical Runge-Kutta 4 schemes are available [15, 16]. For the cell-face reconstruction, we provide weighted essentially non-oscillatory (WENO) schemes and its variants up to order 9 [17, 18]. Choices for approximate Riemann solvers include the Rusanov-flux [14], HLL, and HLLC solver.

Our solver is completely written in JAX [9] which is an updated version of Autograd and XLA. JAX comes with a fully-differentiable version of the popular NumPy package [19] called JAX NumPy. In our implementation we make heavy use of JAX NumPy. The primitive and conservative variable vectors are stored as arrays of size  $(5, n_x + 2n_h, n_y + 2n_h, n_z + 2n_h)$ , where  $(n_x, n_y, n_z)$  is the resolution in the three spatial dimensions and  $n_h$  are the number of halo cells. Halo cells are required to impose boundary conditions. The algorithm naturally degenerates for one- or two-dimensional problems by using a single cell in the excess dimensions.

Atop of the pure numerical computing functionality, JAX provides further function transformations. All compute-intensive routines in our forward-pass are just-in-time compiled via the `jit` function. In order for JAX transformations to work properly, these routines must be expressed as pure functions, i.e. variables that change during the simulation must be passed as function arguments. When using the fluid solver for training and evaluation of ML models, we need tools for differentiation and batch evaluation. For automatic differentiation we use `grad` and `value_and_grad`. Evaluating a batch of simulations in parallel is ensured by the vectorization function `vmap`. Neural networks are built via Haiku [20] and trained via Optax [21].

### 3 Results

#### 3.1 Forward-pass

In this section, classical test-cases for fluid flows exhibiting strong shocks and transition to turbulence are shown. The numerical setup consists of a WENO5-JS [17] cell-face reconstruction combined with a HLLC [14] Riemann solver and a TVD-RK3 [16] integration scheme. The initial and boundary conditions for the following cases are detailed in the appendix A, B, C

##### 3.1.1 Rayleigh-Taylor instability

The (inviscid) Rayleigh-Taylor instability is a gravity driven instability that occurs at the interface between two fluids of different densities when the lighter fluid is pushing the heavier fluid [22]. In Figure 3.1.1, instantaneous density contours for various resolutions are depicted. The use of high-order methods tremendously decreases numerical dissipation. Therefore, floating point errors are no longer hidden by numerical dissipation and result in symmetry-breaking behavior [23]. This effect can be seen for the resolutions  $512 \times 2048$  and  $1024 \times 4096$ .

##### 3.1.2 Taylor-Green Vortex

The (inviscid) Taylor-Green vortex is one of the simplest cases to investigate the generation of small scales and thus the transition from laminar to turbulent flow [24, 25]. In the early stages of the Taylor-Green vortex, the flow field is laminar and strongly anisotropic. Subsequently, energy is transferred to higher wave numbers and the flow becomes turbulent. In Figure 2, we compare the characteristic growth and decay of the dissipation rate for multiple resolutions  $N$  to the DNS of Brachet et al. [24]. Furthermore, the efficiency of our code for this specific test-case is shown.

##### 3.1.3 Double Mach reflection

The Double Mach reflection is a standard test to evaluate the quality of Euler solvers [26]. First suggested by Woodward et al. [27], the case consists of a strong shock hitting a wedge with an inclination of 30 degrees. While the shock travels up the wedge, a self similar structure evolves. In Figure 3, this structure is visualized using the instantaneous density isolines. We simulated this case on a resolution of  $2048 \times 3072$ . Note that the actual height of computational domain is four times higher than what is shown in Figure 3, ensuring that the influence of the north boundary is neglectable.

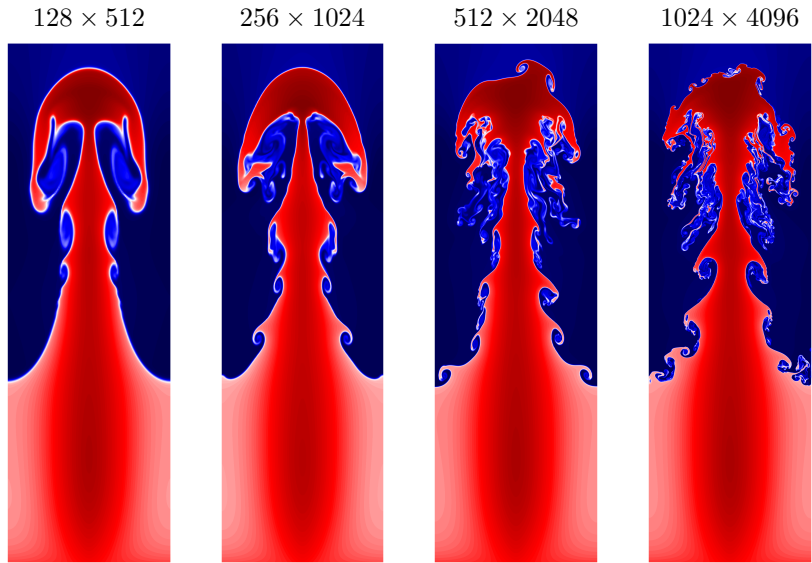


Figure 1: Instantaneous density contours of the Rayleigh-Taylor instability for various resolutions.

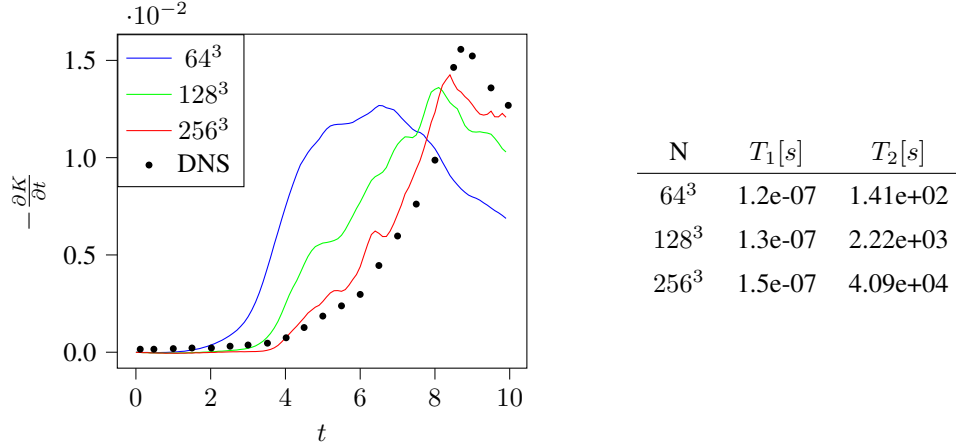


Figure 2: (Left) Rate of turbulence kinetic energy dissipation  $\frac{\partial K}{\partial t}$  with  $K = \frac{1}{2} (\bar{u}^2 + \bar{v}^2 + \bar{w}^2)$  for Taylor-Green vortex. The DNS data is taken from [24]. (Right) Average wall clock time per cell per time step  $T_1$  and wall clock time for entire simulation  $T_2$  on a NVIDIA Quadro P5000.



Figure 3: Instantaneous density isolines of the double Mach reflection.

### 3.2 Backward-pass

Automatic differentiation yields the opportunity to optimize and learn numerical schemes from data by end-to-end optimization through a numerical simulator. As has been done in previous applications, a numerical scheme can be learned by minimizing a loss between a predicted trajectory and a ground truth trajectory. We optimize the popular local Lax-Friedrichs (LxF) flux function (also known as Rusanov flux function) which is defined by

$$\mathbf{F}_{LxF} = \frac{1}{2}(\mathbf{F}_L + \mathbf{F}_R) - \frac{1}{2}\alpha(\mathbf{U}_R - \mathbf{U}_L). \quad (2)$$

Here,  $\mathbf{U}_{L,R}$  and  $\mathbf{F}_{L,R}$  are the left and right sided cell-face reconstructions of the conservatives and flux, respectively, and  $\alpha$  is the scalar numerical viscosity. For the classical Rusanov method the numerical viscosity is defined as  $\alpha_{Rus} = \max |u - c|, |u + c|$ , where  $u$  is the cell-face normal velocity and  $c$  is the local speed of sound. It is well known that although the Rusanov method yields a stable solution without explicitly resolving the interface Riemann problem, the excess numerical diffusion leads to a smeared out solution. As a simple demonstration of the AD-capabilities of our compressible fluid solver, we introduce the Rusanov-NN flux with the dissipation  $\alpha_{Rus}^{NN} = NN(|\Delta u|, u_M, c_M, |\Delta s|)$  to be optimized. The dissipation is output of a multi-layer perceptron which takes as inputs the jump in normal velocity  $\Delta u = |u_R - u_L|$ , the mean normal velocity  $u_M = \frac{1}{2}(u_L + u_R)$ , the mean speed of sound  $c_M = \frac{1}{2}(c_L + c_R)$ , and the entropy jump  $\Delta s = |s_R - s_L|$ .

We set up a highly resolved simulation of an implosion testcase to generate the ground truth trajectory. The high resolution simulation is run on  $128 \times 128$  cells with a WENO5-JS cell-face reconstruction, TVD-RK3 integration scheme, and the HLLC Riemann solver. The initial and boundary conditions

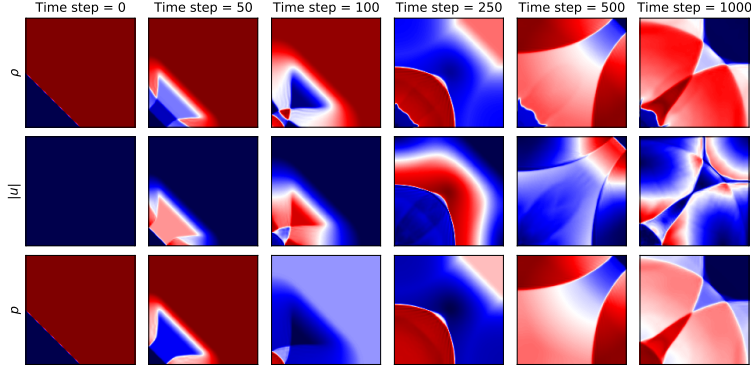


Figure 4: Training data for density, absolute velocity, and pressure at a resolution of  $128 \times 128$ .

are shown in appendix D. A trajectory of 3000 time steps is generated. Exemplary time snapshots for density, absolute velocity, and pressure are visualized in Fig. 4. The left column in Fig. 4 shows the initial condition which is a diagonally placed jump in pressure and density. A shock and a rarefaction wave are emanated from the initial discontinuity and travel along the diagonal  $y = x$ . The shock is propagating towards the lower left corner and is reflected by the walls resulting in a double Mach reflection, while the rarefaction wave is travelling into the open domain. We obtain the ground truth data after coarse-graining onto  $32 \times 32$  points, see top row of Fig. 5.

Here, the ML model is trained in a supervised fashion by minimizing a loss between the coarse-grained (CG) high-resolution simulation (labeled as "Exact" or ground-truth) and the simulation produced by the ML model on a coarse grid. The loss function is defined as the mean-squared error between the predicted and ground truth primitive state vectors  $\tilde{\mathbf{W}} = [\rho, u, v, p]$  and  $\mathbf{W}$  over a trajectory of length  $n_T$ ,

$$L = \frac{1}{n_T} \sum_{i=1}^{n_T} MSE(\mathbf{W}(t_i), \tilde{\mathbf{W}}(t_i)). \quad (3)$$

The training data set consists of the first 2000 time steps of the coarse grained reference solution. During training, the model is unrolled for 15 time steps. We use the Adam optimizer with a constant learning rate  $5e - 4$  and a batch size of 100. The Rusanov-NN model is trained for 1000 epochs. Figure 5 compares the Rusanov and the Rusanov-NN flux function over the full length of a simulation. Although we have trained on trajectories of length 15, we evaluate the model for a much longer trajectory of 3000 time steps. The NN-Rusanov flux stays stable over the course of the simulation and consistently outperforms the Rusanov flux. The ML model even performs very well outside the training set (time steps larger than 2000). The NN-Rusanov flux is less dissipative than the classical Rusanov scheme and recovers small scale flow structures very well, see time step 100 in Fig. 5.

## 4 Conclusion

In this work, a fully-differentiable three-dimensional compressible fluid solver is introduced. Using state-of-the-art high-order numerical methods, the capabilities and efficiency of the code is demonstrated on several classical shock-dominated and turbulent fluid flow test cases. Furthermore, we show that our differentiable solver is capable of end-to-end optimization of neural networks substituting conventional numerical schemes. We believe that fully-differentiable CFD algorithms, written in a rapid-prototyping language as the one presented here, have enormous potential and will enable new avenues of research.

## Acknowledgments and Disclosure of Funding

D.A.B. and A.B.B. thank Steffen J. Schmidt for fruitful discussions.

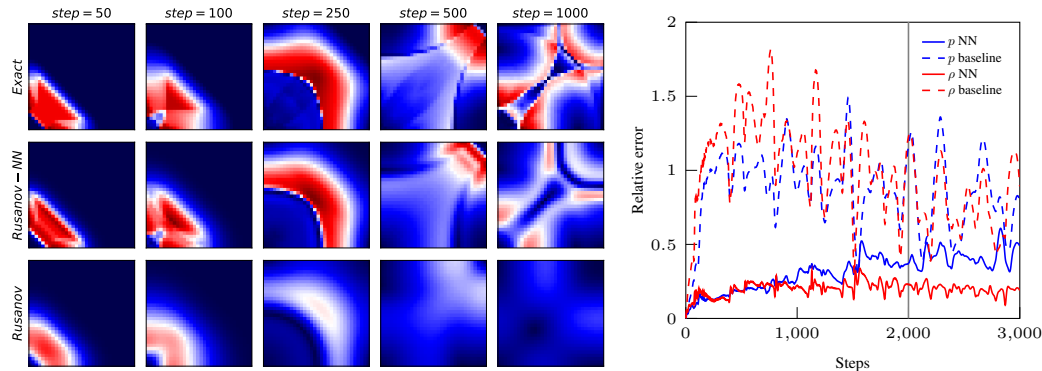


Figure 5: (Left) Absolute velocity fields for the exact (CG  $32 \times 32$ ), ML ( $32 \times 32$ ), and baseline ( $32 \times 32$ ) solvers. (Right) Relative  $L_2$  percentage error for density (red) and pressure (blue). The gray line indicates the training horizon.

This project has received funding from the European Research Council (ERC) under the European Union’s Horizon 2020 research and innovation programme (grant agreement No. 667483).

## References

- [1] Steven L. Brunton, Bernd R. Noack, and Petros Koumoutsakos. Machine Learning for Fluid Mechanics. *Annual Review of Fluid Mechanics*, 52(1):477–508, jan 2020.
- [2] Andrea Beck, David Flad, and Claus Dieter Munz. Deep neural networks for data-driven LES closure models. *Journal of Computational Physics*, 398, 2019.
- [3] H. V. Patel, A. Panda, J. A.M. Kuipers, and E. A.J.F. Peters. Computing interface curvature from volume fractions: A machine learning approach. *Computers and Fluids*, 193, oct 2019.
- [4] Aaron B. Buhendwa, Deniz A. Bezzin, and Nikolaus Adams. Consistent and symmetry preserving data-driven interface reconstruction for the level-set method. *arXiv*, 2021.
- [5] Ben Stevens and Tim Colonius. Enhancement of shock-capturing methods via machine learning. *Theoretical and Computational Fluid Dynamics*, 34(4):483–496, feb 2020.
- [6] Deniz A. Bezzin, Steffen J. Schmidt, and Nikolaus. A. Adams. WENO3-NN: A maximum-order three-point data-driven weighted essentially non-oscillatory scheme. *submitted to J. Comput. Phys.*, 2021.
- [7] Martín Abadi, Paul Barham, Jianmin Chen, Zhifeng Chen, Andy Davis, Jeffrey Dean, Matthieu Devin, Sanjay Ghemawat, Geoffrey Irving, Michael Isard, Manjunath Kudlur, Josh Levenberg, Rajat Monga, Sherry Moore, Derek G Murray, Benoit Steiner, Paul Tucker, Vijay Vasudevan, Pete Warden, Martin Wicke, Yuan Yu, Xiaoqiang Zheng, and Google Brain. TensorFlow: A System for Large-Scale Machine Learning TensorFlow: A system for large-scale machine learning. *Proceedings of the 12th USENIX Symposium on Operating Systems Design and Implementation (OSDI ’16)*, 2016.
- [8] Adam Paszke, Sam Gross, Francisco Massa, Adam Lerer, James Bradbury, Gregory Chanan, Trevor Killeen, Zeming Lin, Natalia Gimelshein, Luca Antiga, Alban Desmaison, Andreas Kopf, Edward Yang, Zach DeVito, Martin Raison, Alykhan Tejani, Sasank Chilamkurthy, Benoit Steiner, Lu Fang, Junjie Bai, and Soumith Chintala. PyTorch: An imperative style, high-performance deep learning library. In *Advances in Neural Information Processing Systems*, volume 32, 2019.
- [9] James Bradbury, Roy Frostig, Peter Hawkins, Matthew James Johnson, Chris Leary, Dougal Maclaurin, George Necula, Adam Paszke, Jake Vander{P}las, Skye Wanderman-{M}ilne, and Qiao Zhang. {JAX}: composable transformations of {P}ython+{N}um{P}y programs, 2018.

- [10] Yohai Bar-Sinai, Stephan Hoyer, Jason Hickey, and Michael P. Brenner. Learning data-driven discretizations for partial differential equations. *Proceedings of the National Academy of Sciences of the United States of America*, 116(31):15344–15349, jul 2019.
- [11] Deniz A. Bezgin, Steffen J. Schmidt, and Nikolaus A. Adams. A data-driven physics-informed finite-volume scheme for nonclassical undercompressive shocks. *Journal of Computational Physics*, 437:110324, mar 2021.
- [12] Samuel S Schoenholz and Ekin D Cubuk. JAX, M.D. A framework for differentiable physics. In *Advances in Neural Information Processing Systems*, volume 2020-Decem, 2020.
- [13] Dmitrii Kochkov, Jamie A Smith, Ayya Alieva, Qing Wang, Michael P Brenner, and Stephan Hoyer. Machine learning accelerated computational fluid dynamics. *Proceedings of the National Academy of Sciences*, 118(21), 2021.
- [14] Eleuterio F. Toro. *Riemann solvers and numerical methods for fluid dynamics a practical introduction*. Springer Verlag, 3rd editio edition, 2009.
- [15] Chi-Wang Shu and Stanley Osher. Efficient implementation of essentially non-oscillatory shock-capturing schemes. *Journal of Computational Physics*, 77:439–471, 1988.
- [16] Sigal Gottlieb and Chi-Wang Shu. Total variation diminishing Runge-Kutta schemes. *Mathematics of computation of the American Mathematical Society*, 67(221):73–85, 1998.
- [17] G.-S. Jiang and Shu. Efficient implementation of weighted ENO schemes. *Journal of Computational Physics*, 126:202–228, 1996.
- [18] Rafael Borges, Monique Carmona, Bruno Costa, and Wai Sun Don. An improved weighted essentially non-oscillatory scheme for hyperbolic conservation laws. *Journal of Computational Physics*, 227(6):3191–3211, mar 2008.
- [19] Charles R Harris, K. Jarrod Millman, Stéfan J van der Walt, Ralf Gommers, Pauli Virtanen, David Cournapeau, Eric Wieser, Julian Taylor, Sebastian Berg, Nathaniel J Smith, Robert Kern, Matti Picus, Stephan Hoyer, Marten H van Kerkwijk, Matthew Brett, Allan Haldane, Jaime Fernández del Río, Mark Wiebe, Pearu Peterson, Pierre Gérard-Marchant, Kevin Sheppard, Tyler Reddy, Warren Weckesser, Hameer Abbasi, Christoph Gohlke, and Travis E Oliphant. Array programming with NumPy, 2020.
- [20] Tom Hennigan, Trevor Cai, Tamara Norman, and Igor Babuschkin. {H}aikū: {S}onnet for {JAX}, 2020.
- [21] Matteo Hessel, David Budden, Fabio Viola, Mihaela Rosca, Eren Sezener, and Tom Hennigan. Optax: composable gradient transformation and optimisation, in JAX!, 2020.
- [22] D. H. Sharp. An overview of Rayleigh-Taylor instability. *Physica D: Nonlinear Phenomena*, 12(1-3):3–18, 1984.
- [23] Nico Fleischmann, Stefan Adami, and Nikolaus A. Adams. Numerical Symmetry-Preserving Techniques for Low-Dissipation Shock-Capturing Schemes. *Computers & Fluids*, 189:94–107, 2019.
- [24] Marc E. Brachet, Daniel I. Meiron, B. G. Nickel, Rudolf H. Morf, Uriel Frisch, and Steven A. Orszag. Small-scale structure of the Taylor-Green vortex. *Journal of Fluid Mechanics*, 130(1983):411–452, 1983.
- [25] M. E. Brachet, D. Meiron, S. Orszag, B. Nickel, R. Morf, and U. Frisch. The Taylor-Green vortex and fully developed turbulence. *Journal of Statistical Physics*, 34(5-6):1049–1063, 1984.
- [26] Friedemann Kemm. On the proper setup of the double Mach reflection as a test case for the resolution of gas dynamics codes. *Computers and Fluids*, 132:72–75, 2016.
- [27] Paul Woodward and Phillip Colella. The numerical simulation of two-dimensional fluid flow with strong shocks, apr 1984.

## A Rayleigh-Taylor instability

The computational domain is  $x, y \in [0, 0.25] \times [0, 1]$ . The initial condition is given by

$$(\rho, u, v, p) = \begin{cases} (2.0, 0.0, -0.025a \cos(8\pi x), 1 + 2y) & \text{if } y \leq 0.5, \\ (1.0, 0.0, -0.025a \cos(8\pi x), 1.5 + y) & \text{if } y > 0.5, \end{cases} \quad (4)$$



with the speed of sound  $a = \sqrt{\gamma p/\rho}$  and the ratio of specific heats  $\gamma = 5/3$ . The east and west boundary conditions are symmetry. The north and south boundary conditions are dirichlet imposing zero velocities  $u$  and  $v$ .

## B Taylor-Green vortex

The computational domain is  $x, y, z \in [0, 2\pi] \times [0, 2\pi] \times [0, 2\pi]$  with periodic boundary conditions for all boundaries. The initial condition is given by

$$\begin{pmatrix} \rho \\ u \\ v \\ w \\ p \end{pmatrix} = \begin{pmatrix} 1.0 \\ \sin(x/L) \cos(y/L) \cos(z/L) \\ -\cos(x/L) \sin(y/L) \cos(z/L) \\ 0.0 \\ \frac{1}{\gamma Ma^2} + \frac{1}{16} (\cos(2x/L) \cos(2y/L) \cos(2z/L)) \end{pmatrix}, \quad (5)$$

with  $\gamma = 1.4$  and  $Ma = 0.1$ .

## C Double Mach reflection

The computational domain is  $x, y \in [0, 4.0] \times [0, 6.0]$ . The initial condition is given by

$$(\rho, u, v, p) = \begin{cases} (\rho_l, u_l, v_l, p_l) & \text{if } y > \sqrt{3} \left(x - \frac{1}{6}\right), \\ (\rho_r, u_r, v_r, p_r) & \text{if } y \leq \sqrt{3} \left(x - \frac{1}{6}\right), \end{cases} \quad (6)$$

with

$$\begin{pmatrix} \rho_l \\ u_l \\ v_l \\ p_l \end{pmatrix} = \begin{pmatrix} 8.0 \\ 7.145 \\ -4.125 \\ 116.5 \end{pmatrix}, \quad \begin{pmatrix} \rho_r \\ u_r \\ v_r \\ p_r \end{pmatrix} = \begin{pmatrix} 1.4 \\ 0.0 \\ 0.0 \\ 1.0 \end{pmatrix}. \quad (7)$$

The north and east boundary conditions impose zero gradients. The west boundary condition is dirichlet imposing  $(\rho_l, u_l, v_l, p_l)$ . The south boundary condition is a combination of dirichlet, imposing  $(\rho_l, u_l, v_l, p_l)$ , and no slip wall.

## D Full Implosion

The initial conditions are given by

$$(\rho, u, v, p) = \begin{cases} (0.14, 0, 0, 0.125) & \text{if } x + y \leq 0.15, \\ (1, 0, 0, 1) & \text{if } x + y > 0.15, \end{cases} \quad (8)$$

on the computational domain  $x, y \in [0, 0.3] \times [0, 0.3]$  with symmetry boundary conditions.